Multivariate Analysis of Coupled Operando EPR/XANES/EXAFS/UV–Vis/ATR-IR Spectroscopy: A New Dimension for Mechanistic Studies of Catalytic Gas-Liquid Phase Reactions

Jabor Rabeah, Valérie Briois, Sven Adomeit, Camille La Fontaine, Ursula Bentrup, Angelika Brückner

Full Paper
doi.org/10.1002/chem.202000436

Spectroscopy

Multivariate Analysis of Coupled Operando EPR/XANES/EXAFS/UV–Vis/ATR-IR Spectroscopy: A New Dimension for Mechanistic Studies of Catalytic Gas-Liquid Phase Reactions

Jabor Rabeah,*[a] Valérie Briois,*[b] Sven Adomeit,[a] Camille La Fontaine,[b] Ursula Bentrup,[a] and Angelika Brückner*[a]

Abstract: Operando EPR, XANES/EXAFS, UV-Vis and ATR-IR spectroscopic methods have been coupled for the first time in the same experimental setup for investigation of unclear mechanistic aspects of selective aerobic oxidation of benzyl alcohol by a Cu/TEMPO catalytic system (TEMPO = 2,2,6,6-tetramethylpiperidinyloxyl). By multivariate curve resolution with alternating least-squares fitting (MCR-ALS) of simultaneously recorded XAS and UV-Vis data sets, it was found that an initially formed (bpy)(NMI)Cu^{I}- complex (bpy = 2,2′-bipyridine, NMI = *N*-methylimidazole) is converted to two different Cu^{II} species, a mononuclear (bpy)(NMI)(CH_3CN)Cu^{II}-OOH species detectable by EPR and ESI-MS, and an EPR-silent dinuclear (CH_3CN)(bpy)(NMI)Cu^{II}(μ-OH)$_2$·Cu^{II}(bpy)(NMI) complex. The latter is cleaved in the further course of reaction into (bpy)(NMI)(HOO)Cu^{II}-TEMPO monomers that are also EPR-silent due to dipolar interaction with bound TEMPO. Both Cu monomers and the Cu dimer are catalytically active in the initial phase of the reaction, yet the dimer is definitely not a major active species nor a resting state since it is irreversibly cleaved in the course of the reaction while catalytic activity is maintained. Gradual formation of non-reducible Cu^{II} leads to slight deactivation at extended reaction times.

Introduction

Selective oxidation reactions of organic compounds over Cu based catalysts using molecular oxygen (or air) have not only potential industrial applications,[1] but are also important in biological systems since Cu/O_2 adducts have been proposed as reactive intermediates in these processes.[2] Therefore, it would be of paramount importance to gain deep understanding of the fundamental aspects, how Cu^{I} complexes activate O_2 and form mono-, di and/or multinuclear Cu-O_2 intermediates that can subsequently facilitate selective substrate oxidation processes.[2d,3] However, this requires the simultaneous application of different spectroscopic techniques together with product analysis, since there is no single method that can provide the whole information necessary. Moreover, using spectroscopic operando techniques individually may give rise to hardly comparable results due to different shapes of spectroscopic cells and reaction conditions (e.g., flow regimes, concentrations, temperature gradients etc.). For these reasons, coupling of complementary operando spectroscopic techniques in the same experiment proved to be very helpful for deriving reliable reaction mechanisms in catalysis.[4] This has been illustrated by impressive examples from both homogeneous and heterogeneous catalysis.[4c,e,5] The main advantage of using such techniques in a coupled setup is to get rid of such deviations, allowing results to be obtained under exactly the same conditions.[4a,6]

A few years ago, we have developed simultaneous operando EPR/UV-Vis/ATR-IR spectroscopy for monitoring selective aerobic oxidation of benzyl alcohol (BzOH) to benzaldehyde (BA),[7] which belongs to the most important reactions for the synthesis of fine chemicals, especially when gaseous O_2 is used instead of environmentally harmful oxidants such as chromate, permanganate or hypochlorite.[1c,8] In particular, Cu complexes with 2,2′-bipyridine (bpy) ligands in combination with *N*-methylimidazole (NMI) and 2,2,6,6-tetramethylpiperidinyloxyl (TEMPO) have been studied extensively as catalytic systems.[9] We used coupled EPR/UV-Vis/ATR-IR spectroscopy to unravel intermediates and active species that had been controversially discussed in literature until that time.[7] Thus, we could follow the fate of paramagnetic Cu^{II} and TEMPO by EPR as well as of diamagnetic Cu^{I} by UV-Vis in parallel with the formation of

[a] Dr. J. Rabeah, S. Adomeit, Dr. U. Bentrup, Prof. Dr. A. Brückner
Leibniz-Institut für Katalyse an der Universität Rostock
Albert-Einstein-Str. 29a, 18059 Rostock (Germany)
E-mail: Jabor.rabeah@catalysis.de
Angelika.bueckner@catalysis.de

[b] Dr. V. Briois, Dr. C. La Fontaine
Synchrotron SOLEIL
L'Orme des Merisiers, BP48, Saint-Aubin, 91192 Gif-sur Yvette (France)
E-mail: valerie.briois@synchrotron-soleil.fr

Supporting information and the ORCID identification number(s) for the author(s) of this article can be found under: https://doi.org/10.1002/chem.202000436.

benzaldehyde by ATR-IR spectroscopy. Based on the combined results, we proposed an active (bpy)(NMI)Cu^{II}-$O_2^{\cdot-}$-TEMPO species formed by electron transfer from a Cu^{I} precursor, in which TEMPO just interacts with $O_2^{\cdot-}$ rather than forming a redox couple with the Cu species.

Nevertheless, recent work by Stahl et al. suggests, based on a combination of X-ray absorption spectroscopy (XAS) techniques and DFT calculations, that TEMPO directly interacts with Cu^{II} via the oxygen atom of TEMPO forming a Cu^{II}-TEMPO complex with Cu^{I}-oxoammonium character.[10] Moreover, recent DFT calculations even suggest that TEMPO remains coordinated to copper during the catalytic cycle.[9f] Actually, the formation of a Cu^{II}-TEMPO complex (with coordination of the N or O atom of TEMPO) has been already proposed in the past,[11] based on DFT calculations,[12] single-crystal X-ray structure,[13] or kinetic studies,[14] but without any evidence for its presence during the catalytic reaction from in situ/operando spectroscopy. Therefore, one open question is whether such a kind of complex does really exist under reaction conditions. Another very important question that could not be answered without doubt in our previous studies was whether a (bpy)Cu^{II}-O-O-Cu^{II}(bpy) dimer (postulated as active intermediate by other groups)[9d,15] is formed, since such a species has been supposed to be EPR-silent.

Therefore we coupled our operando EPR/UV-Vis/ATR-IR setup for the first time simultaneously with time-resolved XANES/EXAFS spectroscopy by placing a small mobile EPR benchtop spectrometer directly into the X-ray beam path of a synchrotron beamline, for which we modified the cavity to host the reactor with implemented UV-Vis and ATR-IR fiber-optical probes, (Figure 1).[16] This bears the advantage that all Cu species in the reaction solution can be visualized. While EPR spectroscopy provides detailed information on paramagnetic species only, that is, on the fate of TEMPO and the structure of single paramagnetic Cu^{II} species, XANES/EXAFS and UV-Vis spectroscopy are generally able to reflect Cu species in all valence and nucleation states, yet frequently in less detail, due to spectral superposition of a variety of different species. Therefore, we used in-depth multivariate curve resolution with alternating least-squares Fitting (MCR-ALS)[17] of XAS and UV-Vis data to gain new mechanistic insights in aerobic oxidation of BzOH to BA, which have not been accessible so far and which may help to clarify still persisting contradictions.

Results and Discussion

Activation molecular oxygen step

As already reported previously, a (bpy)(NMI)Cu^{I}- complex (**1**) (Scheme 1, see below) is formed in situ upon addition of NMI (2 equiv), bpy (1 equiv), and TEMPO (1 equiv) to a solution of Cu^{I}OTf in acetonitrile and the first step of the catalytic cycle is oxidation of this complex by molecular O_2.[7] The formation of complex (**1**) is reflected by a characteristic metal-to-ligand charge-transfer (MLCT) band at 416 nm with a shoulder at 550 nm in the UV-Vis spectrum (Figure 2a, blue line at start), while the EPR spectrum (Figure 2c) shows only the characteristic triplet signal of TEMPO, but no signal from Cu^{I} since it is EPR silent.[7a] The XANES spectrum of this solution shows a resolved shoulder in the rising edge at 8983.0 eV, and an absorption maximum at 8995.2 eV assigned to the 1s→4p transition of Cu^{I} (Figure 2b, blue line at start).[18] One-electron oxidation of Cu^{I} to Cu^{II} by TEMPO to form a Cu^{II}-piperidinoxyl complex was initially proposed by Sheldon et al. based on the stoichiometric oxidation with TEMPO, Hammett correlation, and investigations of kinetic isotope effects.[14] However, our coupled in situ XAS, UV-Vis and EPR results confirm clearly that Cu^{I}OTf is not oxidized by TEMPO under these reaction conditions.

Oxidation of Cu^{I} to Cu^{II} occurs only upon bubbling oxygen into this solution at room temperature. This is evident from a rising Cu^{II} EPR signal at $g_{iso}=2.133$ with hyperfine structure (hfs, $A=66$ G) stemming from the coupling of the unpaired Cu^{II} electron spin (d^9, $S=1/2$) to the nuclear spin of ^{65,63}Cu ($I=3/2$) (Figure 2d).[7] In the UV-Vis spectrum of the same solution (Figure 2a), the MLCT band at 416 nm of Cu^{I} disappears (blue line) and a broad d–d transition band of Cu^{II} arises at 650 nm

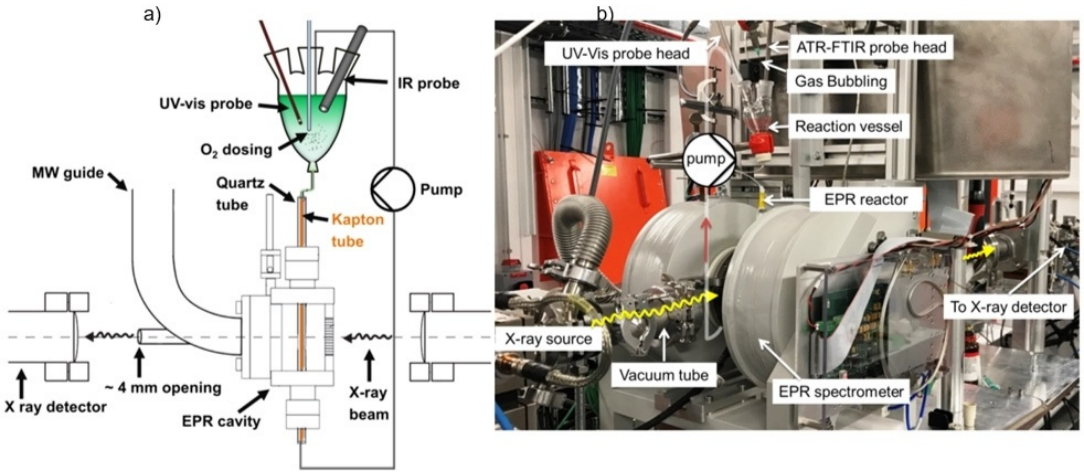

Figure 1. a) Scheme of the operando EPR/XAS/UV-Vis/ATR-IR experimental setup; b) Picture of the setup at the ROCK beamline of the synchrotron facility SOLEIL (Paris).

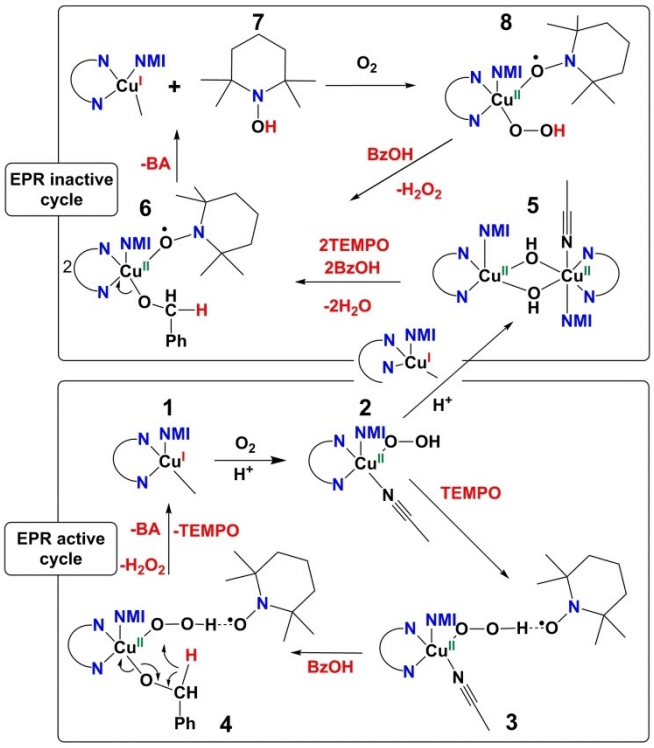

Scheme 1. Pathway for the formation and cleavage of the Cu^{II} dimer during reaction.

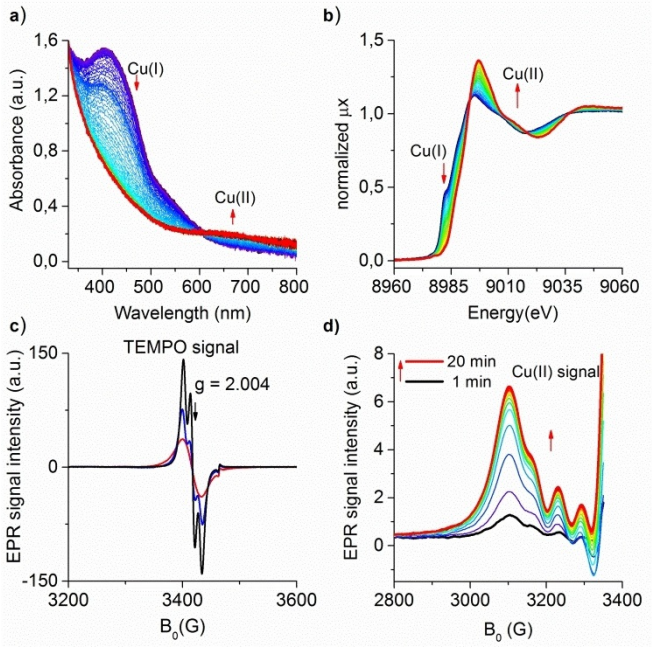

Figure 2. Change with time of a) UV-Vis, b) XANES and d) EPR spectra, of a solution of 25 mM $Cu^{I}OTf$, 1 equiv bpy, 2 equiv NMI and 1 equiv TEMPO in CH_3CN upon bubbling of O_2. c) EPR spectra of TEMPO under Ar before (black line) and after bubbling of O_2 for 20 min (red line) and after addition of BzOH to the above Cu solution (blue line).

(red line).[19] Simultaneously, the Cu^{I} shoulder at 8983.0 eV in the XANES spectra disappears, the absorption maximum is shifted to higher energy (8997.2 eV), the white line rises and a new very weak pre-edge feature appears at 8978 eV (Figure 2b, red line). The latter is assigned to a forbidden 1s→3d transition of Cu^{II} which gains some intensity due to 3d+4p orbital mixing in non-centrosymmetric transition metal ions.[20] The TEMPO EPR signal broadens beyond resolution of the hfs and loses intensity (Figure 2c, red line).

In our previous study,[7a] we have postulated that this is due to weak dipolar interaction of TEMPO with a tentative Cu^{II}-$O_2^{\cdot-}$—TEMPO intermediate as well as with O_2. Actually, the interaction of $O_2^{\cdot-}$ with TEMPO has already been reported,[21] and we confirmed it by recording the EPR spectrum of a TEMPO solution to which KO_2 was added, which showed similar spectral behavior. However, we mentioned that due to its high reactivity, the (bpy)(NMI)Cu^{II}-$O_2^{\cdot-}$ complex could undergo proton abstraction to form an EPR-active (bpy)(NMI)(CH_3CN)Cu^{II}OOH complex (**2**).[7a] Recently, Swarts et al. have found evidence for a $[Cu^{II}OOH]^+$ intermediate by electrospray ionization mass spectrometry analysis (ESI-MS) during aerobic alcohol oxidation in a bis(pyridyl)-*N*-alkylamine/Cu^{I} catalytic system.[22]

In our present work, the formation of complex (**2**) (Scheme 1, see below) has been confirmed by ESI-MS investigations of the pre-oxidized Cu catalyst in the presence and absence of TEMPO. In both cases, an ion at $m/z = 375$ corresponding to complex (**2**) has been detected (Figure 3). This indicates clearly that TEMPO does not directly coordinate to the EPR-active Cu^{II} complex during the activation process as suggested by several authors including recent publications.[9f,10–14]

This is also supported by Figure 4, in which no change of the Cu^{II} EPR signal of complex (**2**) was observed after adding TEMPO (compare black and blue lines). Nevertheless, the inten-

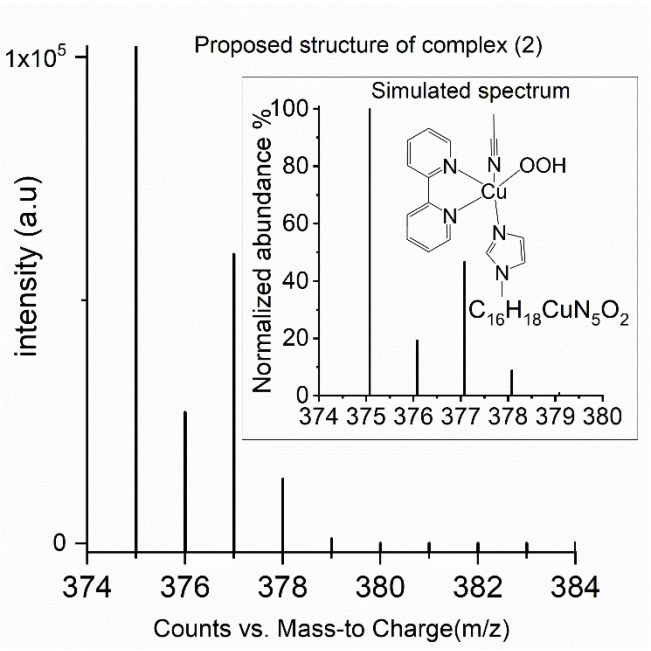

Figure 3. Experimental ESI-MS spectrum for complex (**2**) showing the ion at m/z 375. The inset shows the simulated isotope distribution pattern. Spectrum taken after bubbling O_2 for 20 minutes through a solution containing $Cu^{I}OTf$, 1 equiv bpy, and 2 equiv NMI in CH_3CN.

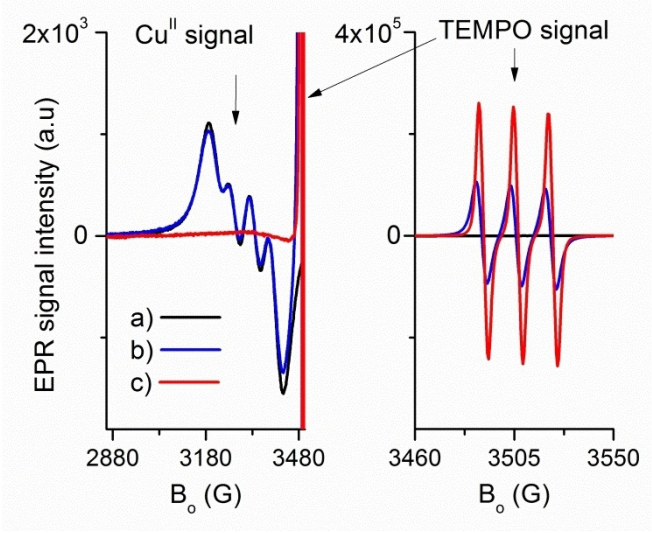

Figure 4. EPR spectra of complex (**2**) formed after bubbling of O_2 for 20 min through 10 mM $Cu^{I}OTf$/bpy/NMI (2 equiv) a) without TEMPO and b) in the presence of 2.5 mM TEMPO in comparison to c) 2.5 mM pure TEMPO in CH_3CN. The solutions were kept under Ar and measured at 20 °C without contact with air.

sity of the TEMPO EPR signal decreased in the presence of complex (**2**). This is clearly evident from a comparison of the red and blue spectra in Figure 4, as well as from a control experiment in which the concentration of TEMPO was kept constant while that of the pre-oxidized Cu complex was varied (Figure S1 in Supporting Information). Since a direct Cu^{II}-TEMPO complex can be ruled out based on the ESI-MS results (Figure 3), a plausible explanation would be the formation of a (bpy)(NMI)(CH_3CN)Cu^{II}OOH-TEMPO intermediate (**3**) (Scheme 1, see below) in which TEMPO gains partial TEMPOH character. Note that for complete TEMPOH formation the EPR signal of TEMPO would disappear.

Spectral behavior during alcohol oxidation

To study the reaction of benzyl alcohol in more detail, BzOH has been added subsequently in four portions of five equivalents to the Cu-TEMPO catalytic system and spectra with all four spectroscopies were recorded as a function of time. To start from a defined steady state, O_2 was bubbled for 20 min through the $Cu^{I}OTf$/bpy/NMI/TEMPO solution before adding the first portion of BzOH. UV-Vis and XAS spectra recorded during BzOH additions are shown in Figures S3–S5 (Supporting Information). Remarkably, no isosbestic point was observed in the UV-Vis spectra after addition of the first three portions of BzOH (see insets in Figure S3). This is in contrast to our previous study, in which an apparent isosbestic point was seen since the total amount of 20 equiv of BzOH had been added in one portion and UV-Vis spectra were recorded only every 6 min.[7a] Comparison of Figure S3 with these previous data illustrates nicely the gain in information enabled by the much higher time resolution of 10 s in the present study. This is also supported by Figure S4 in which our previous experiment with addition of 20 equiv of BzOH in one portion has been repeated, yet with a higher time resolution of 10 s. The lack of isosbestic points in Figure S3 shows clearly that more than two Cu species are involved in the first three successive redox cycles.

The data sets in Figures S3 (UV-Vis) and S5 (XAS) composed of all spectra recorded during bubbling of O_2 and subsequent addition of BzOH to the solution of 25 mM $Cu^{I}OTf$, bpy (1 equiv), NMI (2 equiv) and TEMPO (1 equiv) in CH_3CN were analyzed using the MCR-ALS method,[17,23] to isolate the spectra of pure components involved in the reaction (for details see Supporting Information, section SI-C). It was found that three Cu species were necessary to explain the variance of the UV-Vis and XAS spectra in Figures S3 and S5, respectively. As derived by EXAFS analysis described below, they comprise two mononuclear (Cu^{I} and Cu^{II}) as well as a dinuclear Cu^{II} species. The spectra of these three pure Cu components are plotted in Figure 5 a,b while their concentration profiles as a function of time are shown in Figure 5 c,d. Immediately after adding the first BzOH portion, the signals of both mono- and dinuclear Cu^{II} species disappear in the UV-Vis and XAS spectra (Figure 5 c,d) and the line of a Cu^{I} species, which is almost identical with the initial Cu^{I} signal before adding oxygen (Figure S6), rises to its maximum. At the same time, the EPR signal of Cu^{II} drops to minimum (Figure 5 f, red line), while the TEMPO EPR signal becomes better resolved and increases again (compare the blue line in Figure 2). This had been assigned to the cleavage of the Cu^{II}-OOH-TEMPO intermediate upon oxidation of the alcohol, leading to the formation of diamagnetic Cu^{I} which reduces dipolar interaction with TEMPO.[7] As soon as BzOH is completely converted, the Cu^{I} signal in the XAS and UV-Vis spectra drops suddenly and the Cu^{II} fingerprints reappear again in the spectra of all three spectroscopies (Figure 5). The same behavior is observed after adding the second, third and fourth portion of BzOH.

Mechanistic study

To obtain information on the local environment of Cu, the EXAFS spectra associated with the three MCR-ALS components were analyzed (Table 1, Figure 6, Figure S7 and S8 in Supporting Information). The mononuclear Cu^{I} species (red Fourier Transform (FT) in Figure 6) is satisfactorily reproduced with a 4-fold coordination taking into account single and multiple scattering paths for a Cu(bipy)(NMI)(CH_3CN) model (component 2, Table 1). This is also supported by the fact that the XANES MCR-ALS spectrum of this Cu^{I} component is almost identical with the experimental XANES spectrum of the (bpy)(NMI)Cu^{I}-complex formed initially in a solution of $Cu^{I}OTf$, bpy, NMI and TEMPO in acetonitrile (Figure S6).

This Cu^{I} species is quickly oxidized under O_2 exposure to two Cu^{II} species with similar XANES shape, except for the shoulder after the white line, suggesting different medium range order (Figure 5 b). As a matter of fact, different EXAFS spectra characterized both Cu^{II} species as evidenced by the Fourier transforms presented in Figure 6. Those Cu^{II} species are identified by least-squares fitting analysis as a mononuclear

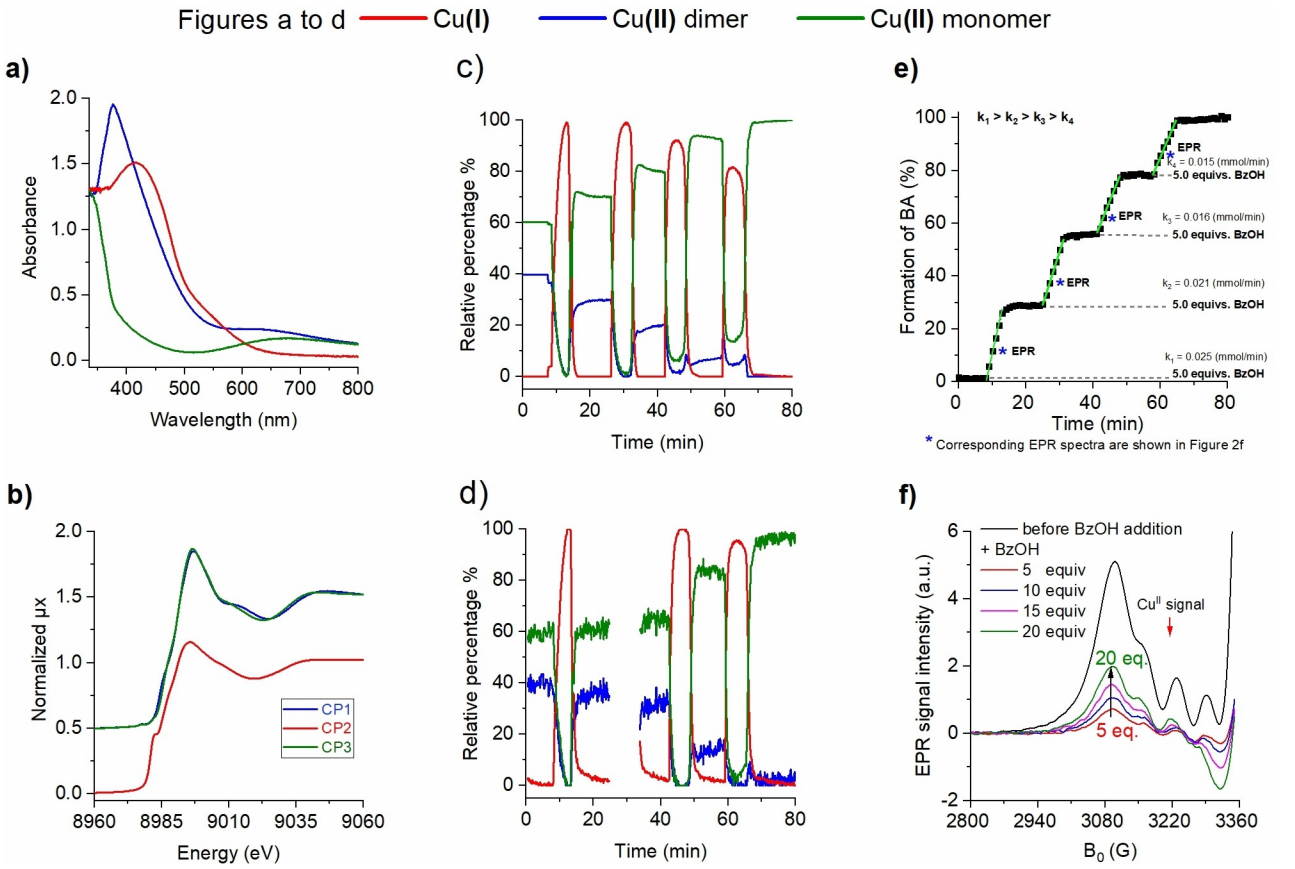

Figure 5. UV-Vis (a) and XAS spectra (b) of the three pure Cu components derived by MCR-ALS, their relative percentage after 20 min exposure to O_2 ($t=0$) and subsequent addition of 4×5 equiv of BzOH to the solution of $Cu^{I}OTf$, bpy, NMI and TEMPO under bubbling of O_2 (c and d), formation of BA derived from the intensity of the ν(C=O) band at 1702 cm^{-1} by ATR-IR (e), and EPR spectra measured at the time marked with * in Figure 5e (f). EPR spectra after reaching the plateaus in plot e are shown in Figure S2.

Table 1. Structural parameters obtained by fitting the EXAFS spectra in Figure 6.

Component	$N^{[a]}$	Atoms[b]	R [Å][c]	$\sigma^2 10^{-3}$ [Å^2][d]	R_f (%) Red-$\chi^{2[e]}$
Cp1	4.2±0.4	O/N	1.94±0.01	5.14±1.3	1.88%
(dinuclear Cu^{II})	1.8±0.7	N	2.41±0.03	2.17±3.8	693
(5)	4.2	C	2.78±0.03	16.0±6.5	
	1	Cu	2.88±0.03	4.46±3.1	
Cp2	4	N	1.99±0.01	7.12±1.1	1.89%
(mononuclear Cu^{I})	2	C	2.81±0.12	17.8±7.1	603
(1)	5	C	2.94±0.12	17.8±7.1	
	10	MS	3.01±0.08	3.84±5.9	
	3	MS	3.20±0.08	3.84±5.9	
Cp3	5	N	1.99±0.01	3.99±1.3	2.06%
(mononuclear Cu^{II})	2	C	2.84±0.05	18.7±15.7	4412
(2)	7	C	2.96±0.06	18.7±15.7	
	12	MS	3.04±0.14	18.8±9.7	
	4	MS	3.10±0.33	18.8±9.7	
	3	MS	3.27±0.09	18.8±9.7	

[a] Coordination numbers were fixed during simulations. [b] O = single scattering by oxygen, N = single scattering by nitrogen, C = single scattering by carbon, MS = multiple scattering paths. [c] R = distance between Cu and the scatterer. [d] σ = Debye Waller factor. [e] Definition of reduced χ^2 and R-factor (R_f) metrics are defined by the IXS standards and criteria committee (http://ixs.iit.edu/subcommittee_reports/sc/err-rep.pdf).

(component 3, green FT) and a dinuclear one (component 1, blue FT) with a second Cu···Cu shell at a distance of 2.88 Å (Table 1). A peroxo-bridged (bpy)(NMI)Cu^{II}-O-O-Cu^{II}(NMI)(bpy) dimer was previously proposed by Stahl et al. as an intermediate, yet without any experimental evidence.[9d] In such peroxo-bridged Cu_2O_2 species, the Cu···Cu distance is usually longer than 3.4 Å.[2a,3e] This, however, does not agree with the value of 2.88 Å obtained from our EXAFS data fitting. Instead, this Cu···Cu distance would be in good agreement with a bis-μ-hydroxo-bridged dinuclear Cu^{II} complex. Thus, a Cu···Cu distance of 2.93 Å was observed for an EPR inactive [(N,N,N)Cu^{II}μ-OH]$_2$ dimer[24] with a very similar Cu^{II} environment, in which Cu coordinates, too, to three N atoms from a ligand. Therefore, we assign the EXAFS spectrum of the dinuclear Cu^{II} component 1 to a (bpy)(NMI)(CH_3CN)Cu^{II}(μ-OH)$_2$$Cu^{II}$(bpy)(NMI) complex (**5**) (Scheme 1, see below). This is also confirmed by ESI-MS analysis (Figure S17) which showed the formation of an ion at m/z = 677 corresponding to complex (**5**).

As indicated by EXAFS, the mononuclear Cu^{II} species is penta-coordinated, yet this method cannot easily distinguish subtle differences in the coordination geometry such as trigonal-bipyramidal and square-pyramidal geometry. This, however, is possible by EPR spectroscopy in a frozen solution, since the principal components of the g-tensor follow a different order,

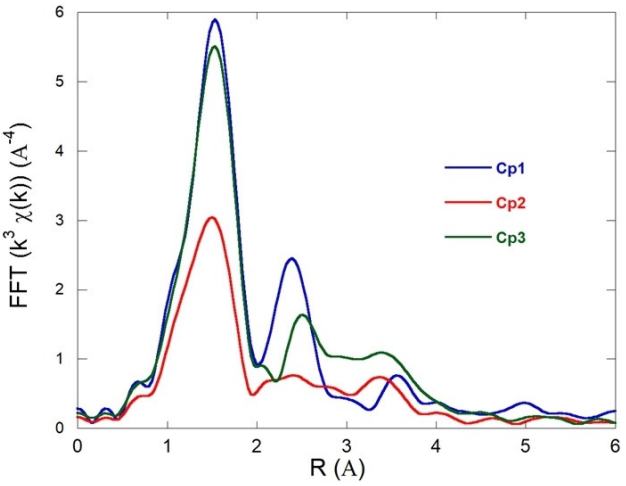

Figure 6. Fourier transformation of the EXAFS spectra (presented in Figure S5) associated with the mononuclear Cu^{I} (red, Cp2), the mononuclear Cu^{II} (green, Cp3) and the dinuclear Cu^{II} (blue, Cp1) pure components derived by MCR-ALS.

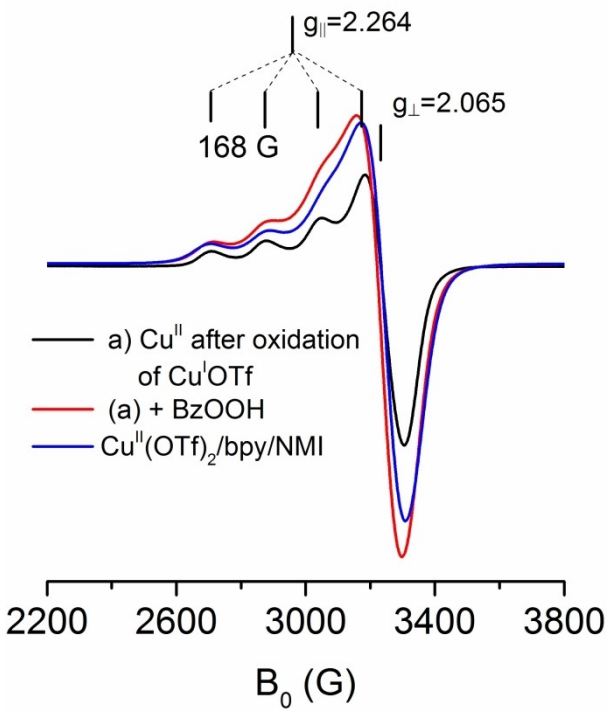

Figure 7. EPR spectra measured at 100 K of a solution containing 25 mM $Cu^{I}OTf$, 1 equiv bpy and 2 equiv NMI in AN after oxidation with O_2 and flushing with Ar (black) and after subsequent addition of 5 equiv BzOOH (red). Reference solution of 25 mM $Cu^{II}(OTf)_2$, 1 equiv bpy and 2 equiv NMI in AN under argon (blue).

namely $g_{\parallel} > g_{\perp} > g_e$ for square-pyramidal and $g_{\perp} > g_{\parallel} \approx g_e$ for trigonal-bipyramidal coordination.[25] In the EPR spectrum of the frozen Cu^{II} containing solution, a signal with $g_{\parallel} = 2.264$ and $g_{\perp} = 2.065$ has been recorded (Figure 7). This indicates clearly that Cu^{II} is in square-pyramidal coordination in the EPR active monomer—information that cannot be obtained from EXAFS alone.

In the UV-Vis spectra, the absorption edge of the dinuclear Cu^{II} species (blue spectrum in Figure 5a) is redshifted compared to the Cu^{II} monomer (green line). Such redshift has been observed for Cu^{II} complexes with increasing steric demand of the ligands.[3e] In our case the bpy and NMI ligands coordinating to Cu^{II} are the same. However, we suppose that the steric hindrance in the Cu dimer might be higher than in the corresponding monomers, due to the connection via two μ-OH bridges and the presence of additional coordinated CH_3CN molecule to one Cu^{II} site. This may give rise to the observed red shift.[3b,e]

After bubbling O_2 for 20 min through the initial solution containing $Cu^{I}OTf$, bpy, NMI and TEMPO, the percentages of the Cu^{II} monomer and dimer derived from XAS and UV-Vis MCR-ALS analysis amount to 60±3 and 40±3%, respectively (Figure 5c,d at $t = 0$). Upon adding BzOH, both Cu^{II} species are immediately reduced to the (bpy)(NMI)Cu^{I}-complex, indicating that both Cu^{II} species are active in oxidizing BzOH to BA (evidenced by ATR-IR, Figure 5e). From the concentration profiles extracted from the MCR-ALS analysis of the UV-Vis and XAS spectra (Figure 5c,d), it is clearly seen that the two different Cu^{II} species (monomeric and dimeric) are converted to the same tetra-coordinated mononuclear Cu^{I} species (**1**) in Scheme 1) and vice versa. Interestingly, the Cu^{II} dimer nearly completely disappears during subsequent addition of the four BzOH portions, leaving behind only mononuclear Cu^{II} at the end of the experiment after conversion of the fourth portion of BzOH. Nevertheless, only a very slight deactivation is observed (Figure 5e), the reason of which will be discussed below. This shows that the bis-μ-hydroxo-bridged dinuclear Cu^{II} complex **5** is an active species at the early stage of the reaction, but it is gradually cleaved into Cu^{II} monomers which govern catalytic activity in due course.

A tentative pathway for the formation and conversion of the dimer is shown in Scheme 1. Previously we have shown that the initial (bpy)(NMI)Cu^{I}-complex (**1**) activates oxygen by transfer of one electron and formation of an active Cu^{II} superoxo species[7a] which is stabilized by abstraction of a proton to form **2** as evident from ESI-MS analysis. This species interacts with TEMPO to form **3**. Intermediate **3** oxidizes the alcohol, liberates TEMPO again and transforms back into the starting Cu^{I} complex (**1**) that can then enter into a new redox cycle. A part of this, complex **2** can obviously react with another molecule of complex **1** to form the bis-μ-hydroxo-bridged dinuclear Cu^{II} species **5**, possibly by passing a peroxo bridged intermediate that has also been postulated in other works.[19] **5** is cleaved by reaction with alcohol and TEMPO to form complex **6** which then releases the aldehyde and forms the EPR-silent Cu^{I} complex **1** and TEMP-OH **7**.[9f]

Stahl et al. have shown that the interaction of the (bpy)(NMI)Cu^{I}-complex **1** with TEMP-OH **7** in the presence of O_2 leads to the formation of (bpy)(NMI)Cu^{II}OH and TEMPO.[9d] Since both species are paramagnetic, one should expect an increase in EPR intensity during subsequent addition of BzOH portions and cleavage of the Cu^{II} dimer **5**, given the latter is EPR-silent, due to antiferromagnetic coupling of the two Cu^{II} electron spins. EPR-silence of such a dimer has been postulat-

ed in quite some papers[3e,19,26] and is also supported by the experiment shown in Figure 7. The EPR signal intensities (double integral) in an in situ oxidized $Cu^{I}OTf$/bpy/NMI solution (in which the dimer **5** is shown to be formed) is lower than that of a complex formed by mixing $Cu^{II}(OTf)_2$ with bpy and NMI in the same concentrations (compare to black and blue spectrum in Figure 7). It is evident that in the former case only 52% of the total Cu amount contributes to the Cu^{II} EPR signal. As both UV-Vis and XAS spectroscopy indicate complete oxidation of Cu^{I} to Cu^{II} (Figure 5c,d), this means that ≈48% of Cu^{I} must be oxidized to an EPR-silent Cu^{II} species, which might be the Cu^{II} dimer **5** as evident from ESI-MS analysis (Figure S17). This agrees roughly with the results of the MCR-ALS analysis, in which around 40% of the total copper in the pre-oxidized $Cu^{I}OTf$/bpy/NMI solution was found as Cu^{II} dimer (Figure 5c,d). An indirect evidence for the EPR-silence of this dimer was also obtained from a reference experiment: When benzoic acid (BzOOH) was added to a $Cu^{I}OTf$/bpy/NMI solution after oxidation with O_2 and flushing with argon, an almost twofold increase of the Cu^{II} EPR signal intensity was observed (compare to black and red spectrum in Figure 7). This is due to the cleavage of the EPR-silent dimer **5** and formation of an EPR-active mononuclear Cu^{II} complex.

Consequently, we should have observed a gradual increase of the total Cu^{II} EPR signal intensity with time when the antiferromagnetic dimer **5** is cleaved during the experiment shown in Figure 5. This was, however, not the case. Instead, the Cu^{II} EPR intensity after subsequent addition of the 4× 5 equivalents of BzOH and saturation of the reaction solution with O_2 remained almost constant (Figure S2). Since we have clear evidence for the formation of an EPR-silent Cu^{II} dimer **5** from simultaneously recorded EXAFS and EPR spectra as well as from ESI-MS analysis, we must conclude that this species is converted to an EPR-silent Cu^{II} monomer which does not contribute to the total Cu^{II} EPR signal recorded during the experiment in Figure 5. Therefore, we propose that the interaction of **5** with TEMPO (Scheme 1) leads to the formation of a mononuclear Cu^{II}-TEMPO complex **6** which might be EPR-silent, due to strong dipolar interaction between Cu^{II} and the coordinated TEMPO species, both being paramagnetic. Very recently, such a kind of complex with direct bonding between the oxygen atom of TEMPO and the Cu^{II} site has been postulated, yet without coordination of NMI to the Cu center.[9f,10] In light of the EXAFS results, we suggest that the fifth coordination site at Cu^{II} is occupied by NMI, which is known to enhance the Cu^{I} redox potential.[7b] This is also in line with our previous UV-Vis and EPR results showing clearly that NMI coordinates to Cu^{II} when it is present in solution.[7a] However, we cannot completely rule out coordination of other ligand such CH_3CN. Obviously, species **6** is only formed in the presence of BzOH, since direct interaction of Cu^{II} and TEMPO was not observed when TEMPO was added to complex **2** alone (see above).

Reason for deactivation

During reaction with the subsequently added four portions of BzOH a slight deactivation was observed. The time to reach the maximum yield of BA (derived from the intensity of the ν(C=O) band of BA in the ATR-IR spectrum) increases from 6 min after adding the first portion of 5 equiv BzOH to 8 min after adding the last portion (Figure 5e). The reason for this may be the formation of a small amount of non-reducible Cu^{II} (Scheme 2) that cannot enter into a new catalytic cycle

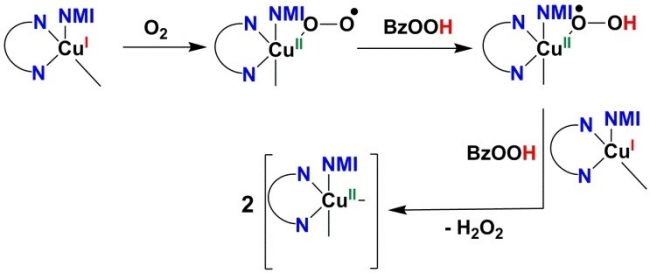

Scheme 2. Tentative pathway for the formation of inactive, non-reducible Cu^{II} species during the catalytic reaction.

(Scheme 1). This is evident from the EPR spectra recorded immediately after adding a portion of BzOH (Figure 5f). The Cu^{II} signal vanishes almost completely when the first portion is added due to reduction of the active species (**4** in Scheme 1, red line in Figure 5f). With each further BzOH addition there remains an increasing amount of Cu^{II} that cannot be reduced to Cu^{I} again (evident from the rising Cu^{II} EPR signal in Figure 5f). This behavior is also fully confirmed by the MCR-ALS analysis of the UV-Vis data showing a slight decrease of the converted amount of Cu^{I} species after the third and the fourth BzOH addition, passing from 98 to 92% and finally 82% (Figure 5c). We suppose that this non-reducible Cu^{II} may arise from partial oxidation of BzOH to BzOOH which reacts with the active $[(bpy)(NMI)Cu^{II}O_2]$ intermediate to a $(bpy)(NMI)Cu^{II}$-OOBz site that cannot activate gaseous O_2 anymore, since transfer of an electron like in step 1 of Scheme 1 is no longer possible (Scheme 2). This assumption has been confirmed by an experiment in which 1 equiv of BzOOH was added to the reaction mixture containing the active Cu complex, which led to no conversion of BzOH to BA.[7b] The formation of BzOOH was detected by Gas Chromatography analysis of the product after the catalytic test but not by operando ATR-IR, probably due to its low concentration.

Proposed reaction mechanism

Consequently, the results of the three coupled techniques suggest that there are two pathways for selective alcohol oxidation to aldehyde (Scheme 1). One comprises mononuclear EPR-active Cu^{II} complexes (**1**→**2**→**3**→**4**→**1**) and the other passes through a dinuclear copper intermediate (**5**) leading to formation of a mononuclear EPR-inactive copper-TEMPO complex (**6**→**1** and **7**→**8**→**6**). Both pathways are catalytically active since we only observed a negligible deactivation during the catalytic test (Figure 5e). Possibly the cycle **1**→**2**→**3**→**4**→**1** is

very fast in the presence of TEMPO, so that formation of the dimer **5** is suppressed with increasing reaction time.

Conclusions

In this work, we have for the first time used simultaneous operando EPR/XANES/EXAFS/UV-Vis/ATR-IR spectroscopy to investigate the still controversially discussed structure and role of active sites in Cu/TEMPO catalyzed selective aerobic benzyl alcohol oxidation. It was found that a tetracoordinated (bpy)-(NMI)Cu^{I}-complex, formed in situ at the start of the reaction, is initially converted to two different Cu^{II} species, an EPR-active mononuclear (bpy)(NMI)(CH_3CN)Cu^{II}-OOH species and an EPR-silent dinuclear (bpy)(NMI)Cu^{II}(μ-OH)$_2$$Cu^{II}$(bpy)(NMI)($CH_3CN$) complex. This dinuclear species is cleaved during reaction into (bpy)(NMI)(OOH)Cu^{II}-TEMPO monomers that are also EPR-silent due to antiferromagnetic interaction between Cu^{II} and TEMPO but govern, besides (bpy)(NMI)(CH_3CN)Cu^{II}OOH—TEMPO, the catalytic activity in due course. Though the Cu^{II} dimer obviously participates in the initial phase of the reaction, it is definitely not a major active species nor a resting state since it is irreversibly dissolved into monomers. This results in two parallel catalytically active Cu^{I}/Cu^{II} redox cycles (Scheme 1), one detectable by EPR and the other not, which differ in their mode of coordinating TEMPO. Both cycles contribute almost equally to catalytic activity.

We have clearly demonstrated the added value of extending our previous simultaneous EPR/UV-Vis/ATR-IR technique by coupling with XANES/EXAFS, in comparison to separate experiments. While XAS and UV-Vis spectroscopy can detect both Cu^{II} monomer and dimer species as well as both valence states of Cu, their ability to reflect the precise coordination geometry of Cu is limited, in particular for XAS without complete full multiple scattering simulations of XANES. This limitation is compensated by EPR, at least in the case of Cu^{II}. On the other hand, EPR can neither detect Cu^{I} nor distinguish between mono- and dinuclear Cu^{II} when both Cu^{II} ions interact only weakly without forming a $S=1$ spin system, while antiferromagnetic coupling prevents detection of Cu^{II} completely. This drawback can be overcome by EXAFS.

Finally, it should be mentioned that the new coupling technique is not limited to homogeneous catalytic gas-liquid phase reactions at room temperature, such as Cu/TEMPO catalyzed alcohol oxidation used as example in this work. It has broader application potential also for heterogeneous catalytic gas-phase reactions, since the flow reactor can be heated and used with a solid catalyst.[16] Moreover, our setup can be easily assembled at different synchrotron radiation facility beamlines depending on the requirements of the systems to be studied.

Experimental Section

The experimental setup for coupled operando EPR/XAS/UV-Vis/ATR-IR spectroscopy is shown in Figure 1. A Kapton capillary (inner diameter 1 mm) is used as a flow reactor. It is stabilized by implementing it into a quartz tube mantle with two opposite holes covered by kapton foil to allow the X-ray beam to pass through. This reactor was mounted in the cavity of a small benchtop cw-EPR spectrometer (EMXnano, Bruker). The cavity of the EPR spectrometer has been modified accordingly and installed directly in the beam path of the ROCK quick-EXAFS beamline (SOLEIL, Paris).[27] The top of the EPR reactor is connected to a three necked glass reservoir equipped with a capillary for bubbling oxygen or inert gas (N_2) into the solution, and with fiber-optical immersion probes for simultaneous recording of UV-Vis and ATR-IR spectra. The flow reactor is connected to a nano-pump (DURATEC Analysentechnik GmbH) for circulation of the reaction mixture through the reactor within the EPR cavity.

Operando ATR-IR spectra were collected by a ReactIR 15 spectrometer (Mettler-Toledo) in an interval of 60 s using an AgX fiber-optical immersion probe with a diamond crystal as ATR element in the range between 650 and 1900 cm^{-1}. Quantification was performed by integration of the ν(C=O) band between 1670 and 1743 cm^{-1} without baseline correction using a calibration sequence.

UV-Vis spectra in the range of 200–800 nm were recorded by a Varian Cary 50 dual beam apparatus equipped with a pulsed Xenon lamp and a Si diode detector. A Hellma immersion probe with an optical path of 1 mm was used for collecting the data. Spectra were measured with a scan rate of 4800 nm min^{-1} and a cycle time of 10 s which corresponds to the time between two consecutive spectra. No baseline correction was applied, but the spectrum of the acetonitrile solvent recorded under the same conditions has been subtracted.

Operando EPR spectra were recorded with a microwave power of 6.9 mW, a modulation frequency of 100 kHz and a modulation amplitude up to 5G. For recording EPR spectra at low temperature (100 K), an EMXmicro X-band EPR spectrometer equipped with a variable temperature control unit including a liquid N_2 cryostat and a temperature controller was used. In some cases, EPR measurements alone have been repeated on a Bruker ELEXSYS 500 spectrometer equipped with a high sensitivity resonator under the same reaction conditions. This led to the same results, yet with better spectral resolution that facilitated spectra interpretation. This is the reason why certain EPR figures presented herein have a different intensity scale.

XANES and EXAFS spectra were recorded in transmission mode using three ionization chambers filled with 1 bar of N_2 gas. A Si(111) channel-cut crystal was used as monochromator with an oscillation amplitude of 2.1° and an oscillation frequency of 2 Hz. During monochromator oscillation, two 250 ms spectra were recorded, one with increasing and one with decreasing Bragg angles. In further data processing, only the former was considered. Harmonic rejection was done using two mirrors coated with B_4C which surrounded the monochromator and accepted the pink and monochromatized beam at 2.75 mrad of incidence, respectively. The beam size at the sample position was 0.4 mm (H) x 0.2 mm (V) (FWHM). A copper metal foil was recorded permanently and simultaneously with the data of interest using the third ionization chamber.

XAS data normalization was performed using the Python normal_ GUI graphical interface developed at SOLEIL for the fast handling of the Quick-XAS data.[28] Energy calibration was performed at the first derivative maximum of the spectrum of the Cu metal foil (8979 eV). 20 spectra recorded with increasing angles were merged in order to improve the signal to noise ratio. This led to a time resolution of 10 s between two consecutive spectra. UV-Vis and XAS spectra have been analyzed by multivariate curve resolution with alternating least-squares fitting (MCR-ALS).[17,23] Details of this procedure are described in the Supporting Information, section SI-C.

Low-resolution mass spectrometry investigations were performed using electron spray ionization mass spectrometry (ESI) (Agilent technologies 6130 Quadrupole LCMS).

Acknowledgements

We thank G. Agostini, T. H. Vuong and M. Klahn for experimental support and discussions. In memoriam of Prof. Reinhard Stößer we are grateful for his help in developing the experimental setup. The measurements at ROCK beamline-SOLEIL were supported by a public grant overseen by the French National Research Agency (ANR) as part of the "Investissements d'Avenir" program (reference: ANR10-EQPX45).

Conflict of interest

The authors declare no conflict of interest.

Keywords: ATR-IR · coupled operando spectroscopy · EPR · EXAFS · reaction mechanism · XANES

[1] a) E. J. Corey, J. W. Suggs, *Tetrahedron Lett.* **1975**, *16*, 2647 – 2650; b) D. B. Dess, J. C. Martin, *J. Org. Chem.* **1983**, *48*, 4155 – 4156; c) O. Das, T. K. Paine in *Transition Metal Catalysis in Aerobic Alcohol Oxidation*, RSC Publishing, Cambridge, **2015**, pp. 40 – 69.

[2] a) E. A. Lewis, W. B. Tolman, *Chem. Rev.* **2004**, *104*, 1047 – 1076; b) J. W. Whittaker, *Chem. Rev.* **2003**, *103*, 2347 – 2364; c) F. Wendt, M. Rolff, W. Thimm, C. Näther, F. Tuczek, *Z. Anorg. Allg. Chem.* **2013**, *639*, 2502 – 2509; d) M. Rolff, J. Schottenheim, H. Decker, F. Tuczek, *Chem. Soc. Rev.* **2011**, *40*, 4077 – 4098; e) E. I. Solomon, P. Chen, M. Metz, S.-K. Lee, A. E. Palmer, *Angew. Chem. Int. Ed.* **2001**, *40*, 4570 – 4590; *Angew. Chem.* **2001**, *113*, 4702 – 4724; f) A. G. Blackman, W. B. Tolman in *Metal-Oxo and Metal-Peroxo Species in Catalytic Oxidations* (Ed.: B. Meunier), Springer, Heidelberg, **2000**, pp. 179 – 211; g) S. Ferguson-Miller, G. T. Babcock, *Chem. Rev.* **1996**, *96*, 2889 – 2907.

[3] a) M. Schatz, V. Raab, S. P. Foxon, G. Brehm, S. Schneider, M. Reiher, M. C. Holthausen, J. Sundermeyer, S. Schindler, *Angew. Chem. Int. Ed.* **2004**, *43*, 4360 – 4363; *Angew. Chem.* **2004**, *116*, 4460 – 4464; b) E. I. Solomon, F. Tuczek, D. E. Root, C. A. Brown, *Chem. Rev.* **1994**, *94*, 827 – 856; c) E. I. Solomon, M. J. Baldwin, M. D. Lowery, *Chem. Rev.* **1992**, *92*, 521 – 542; d) D. A. Quist, D. E. Diaz, J. J. Liu, K. D. Karlin, *J. Biol. Inorg. Chem.* **2017**, *22*, 253 – 288; e) L. M. Mirica, X. Ottenwaelder, T. D. P. Stack, *Chem. Rev.* **2004**, *104*, 1013 – 1045; f) K. D. Karlin, S. Kaderli, A. D. Zueberbuehler, *Acc. Chem. Res.* **1997**, *30*, 139 – 147; g) S. E. Allen, R. R. Walvoord, R. Padilla-Salinas, M. C. Kozlowski, *Chem. Rev.* **2013**, *113*, 6234 – 6458.

[4] a) M. A. Banares, *Catal. Today* **2005**, *100*, 71 – 77; b) M. A. Banares, *Top. Catal.* **2009**, *52*, 1301 – 1302; c) A. M. Beale, J. P. Hofmann, M. Sankar, E. M. Schrojenstein Lantman, B. M. Weckhuysen in *Heterogeneous Catalysts for Clean Technology*, Wiley-VCH, Weinheim, **2013**, pp. 365 – 411; d) A. M. Beale, A. M. J. van der Eerden, K. Kervinen, M. A. Newton, B. M. Weckhuysen, *Chem. Commun.* **2005**, 3015 – 3017; e) A. Brückner, *Chem. Commun.* **2005**, 1761 – 1763; f) A. Chakrabarti, M. E. Ford, D. Gregory, R. Hu, C. J. Keturakis, S. Lwin, Y. Tang, Z. Yang, M. Zhu, M. A. Banares, I. E. Wachs, *Catal. Today* **2017**, *283*, 27 – 53; g) B. M. Weckhuysen, *Phys. Chem. Chem. Phys.* **2003**, *5*, 4351 – 4360.

[5] a) U. Bentrup, *Chem. Soc. Rev.* **2010**, *39*, 4718 – 4730; b) A. Vimont, F. Thibault-Starzyk, M. Daturi, *Chem. Soc. Rev.* **2010**, *39*, 4928 – 4950; c) Y. Zhang, D. Fu, X. Xu, Y. Sheng, J. Xu, Y.-f. Han, *Curr. Opin. Chem. Eng.* **2016**, *12*, 1 – 7; d) S. P. Verkleij, G. T. Whiting, S. P. Esclapez, M. M. Mertens, A.-J. Bons, M. Burgers, B. M. Weckhuysen, *Catal. Sci. Technol.* **2018**, *8*, 2175 – 2185; e) J. J. Bravo-Suárez, P. D. Srinivasan, *Catal. Rev.* **2017**, *59*, 295 – 445; f) R. Chung, J. E. Hein, *Top. Catal.* **2017**, *60*, 594 – 608; g) V. Briois, D. Lützenkirchen-Hecht, F. Villain, E. Fonda, S. Belin, B. Griesebock, R. Frahm, *J. Phys. Chem. A* **2005**, *109*, 320 – 329; h) A. Rochet, B. Baubet, V. Moizan, E. Devers, A. Hugon, C. Pichon, E. Payen, V. Briois, *J. Phys. Chem. C* **2017**, *121*, 18544 – 18556; i) A. R. Passos, C. La Fontaine, L. Martins, S. H. Pulcinelli, C. V. Santilli, V. Briois, *Catal. Sci. Technol.* **2018**, *8*, 6297 – 6301; j) T. A. Nijhuis, S. J. Tinnemans, T. Visser, B. M. Weckhuysen, *Phys. Chem. Chem. Phys.* **2003**, *5*, 4361 – 4365; k) R. Pérez Vélez, I. Ellmers, H. Huang, U. Bentrup, V. Schünemann, W. Grünert, A. Brückner, *J. Catal.* **2014**, *316*, 103 – 111; l) J. Rabeah, M. Bauer, W. Baumann, A. E. C. McConnell, W. F. Gabrielli, P. B. Webb, D. Selent, A. Bruckner, *ACS Catal.* **2013**, *3*, 95 – 102; m) J. Rabeah, J. Radnik, V. Briois, D. Maschmeyer, G. Stochniol, S. Peitz, H. Reeker, C. La Fontaine, A. Brückner, *ACS Catal.* **2016**, *6*, 8224 – 8228; n) A. Rochet, V. Moizan, F. Diehl, C. Pichon, V. Briois, *Catal. Today* **2013**, *205*, 94 – 100; o) T. H. Vuong, S. Bartling, U. Bentrup, H. Lund, J. Rabeah, H. Atia, U. Armbruster, A. Brueckner, *Catal. Sci. Technol.* **2018**, *8*, 6360 – 6374; p) T. H. Vuong, J. Radnik, J. Rabeah, U. Bentrup, M. Schneider, H. Atia, U. Armbruster, W. Gruenert, A. Brueckner, *ACS Catal.* **2017**, *7*, 1693 – 1705; q) X. Li, X. Yang, J. Zhang, Y. Huang, B. Liu, *ACS Catal.* **2019**, *9*, 2521 – 2531; r) F. Wang, J. Z. Jiang, B. Wang, *Catalysts* **2019**, *9*, 477.

[6] a) V. Briois, S. Belin, F. Villain, F. Bouamrane, H. Lucas, R. Lescouëzec, M. Julve, M. Verdaguer, M. S. Tokumoto, C. Santilli, S. H. Pulcinelli, X. Carrier, J. M. Krafft, C. Jubin, M. Che, *Phys. Scr.* **2005**, 38; b) A. Urakawa, *Curr. Opin. Chem. Eng.* **2016**, *12*, 31 – 36; c) *Recent Developments in Operando Spectroscopy* (Ed.: A. Brueckner), Elsevier, Amsterdam, **2010**.

[7] a) J. Rabeah, U. Bentrup, R. Stößer, A. Brückner, *Angew. Chem. Int. Ed.* **2015**, *54*, 11791 – 11794; *Angew. Chem.* **2015**, *127*, 11957 – 11960; b) S. Adomeit, J. Rabeah, A. E. Surkus, U. Bentrup, A. Brueckner, *Inorg. Chem.* **2017**, *56*, 684 – 691.

[8] R. O. C. Norman, J. M. Coxon, *Principles of Organic Synthesis, 3rd ed.*, Blackie Academic & Professional, London, **1993**.

[9] a) S. Albonetti, R. Mazzoni, F. Cavani in *Transition Metal Catalysis in Aerobic Alcohol Oxidation*, The Royal Society of Chemistry, Cambridge **2015**, pp. 1 – 39; b) J. M. Hoover, S. S. Stahl, *J. Am. Chem. Soc.* **2011**, *133*, 16901 – 16910; c) B. L. Ryland, S. S. Stahl, *Angew. Chem. Int. Ed.* **2014**, *53*, 8824 – 8838; *Angew. Chem.* **2014**, *126*, 8968 – 8983; d) J. M. Hoover, B. L. Ryland, S. S. Stahl, *J. Am. Chem. Soc.* **2013**, *135*, 2357 – 2367; e) J. M. Hoover, B. L. Ryland, S. S. Stahl, *ACS Catal.* **2013**, *3*, 2599 – 2605; f) M. A. Iron, A. M. Szpilman, *Chem. Eur. J.* **2017**, *23*, 1368 – 1378; g) M. Carbó López, P. Y. Chavant, F. Molton, G. Royal, V. Blandin, *ChemistrySelect* **2017**, *2*, 443 – 450.

[10] R. C. Walroth, K. C. Miles, J. T. Lukens, S. N. MacMillan, S. S. Stahl, K. M. Lancaster, *J. Am. Chem. Soc.* **2017**, *139*, 13507 – 13517.

[11] a) P. Gamez, I. W. C. E. Arends, R. A. Sheldon, J. Reedijk, *Adv. Synth. Catal.* **2004**, *346*, 805 – 811; b) P. Gamez, I. W. C. E. Arends, J. Reedijk, R. A. Sheldon, *Chem. Commun.* **2003**, 2414 – 2415.

[12] a) L. Cheng, J. Wang, M. Wang, Z. Wu, *Inorg. Chem.* **2010**, *49*, 9392 – 9399; b) P. Belanzoni, C. Michel, E. J. Baerends, *Inorg. Chem.* **2011**, *50*, 11896 – 11904.

[13] J. Laugier, J. M. Latour, A. Caneschi, P. Rey, *Inorg. Chem.* **1991**, *30*, 4474 – 4477.

[14] A. Dijksman, I. W. C. E. Arends, R. A. Sheldon, *Org. Biomol. Chem.* **2003**, *1*, 3232 – 3237.

[15] Z. Z. Liu, Z. Q. Shen, N. Zhang, W. Zhong, X. M. Liu, *Catal. Lett.* **2018**, *148*, 2709 – 2718.

[16] J. Rabeah, S. Adomeit, A. Brücker, WO 2019154488 A1, **2018**.

[17] a) A. de Juan, J. Jaumot, R. Tauler, *Anal. Methods* **2014**, *6*, 4964 – 4976; b) M. Garrido, F. X. Rius, M. S. Larrechi, *Anal. Bioanal. Chem.* **2008**, *390*, 2059 – 2066 and references therein; c) A. Voronov, A. Urakawa, W. van Beek, N. E. Tsakoumis, H. Emerich, M. Rønning, *Anal. Chim. Acta* **2014**, *840*, 20 – 27; d) W. H. Cassinelli, L. Martins, A. R. Passos, S. H. Pulcinelli, C. V. Santilli, A. Rochet, V. Briois, *Catal. Today* **2014**, *229*, 114 – 122; e) A. Rochet, B. Baubet, V. Moizan, C. Pichon, V. Briois, *C. R. Chim.* **2016**, *19*, 1337 – 1351; f) A. Martini, E. Borfecchia, K. A. Lomachenko, I. A. Pankin, C. Negri, G. Berlier, P. Beato, H. Falsig, S. Bordiga, C. Lamberti, *Chem. Sci.* **2017**, *8*, 6836 – 6851.

[18] S. Zhu, S. Liang, Y. Tong, X. An, J. Long, X. Fu, X. Wang, *Phys. Chem. Chem. Phys.* **2015**, *17*, 9761 – 9770.

[19] N. Kitajima, Y. Moro-oka, *Chem. Rev.* **1994**, *94*, 737 – 757.

[20] a) E. Asato, S. Hashimoto, N. Matsumoto, S. Kida, *J. Chem. Soc. Dalton Trans.* **1990**, 1741 – 1746; b) G. L. Woolery, L. Powers, M. Winkler, E. I. Solomon, K. Lerch, T. G. Spiro, *Biochim. Biophys. Acta Protein Struct. Mol. Enzymol.* **1984**, *788*, 155 – 161.

[21] K. Takeshita, S. Okazaki, A. Itoda, *Anal. Chem.* **2013**, *85*, 6833 – 6839.
[22] L. Marais, J. Burés, J. H. L. Jordaan, S. Mapolie, A. J. Swarts, *Org. Biomol. Chem.* **2017**, *15*, 6926 – 6933.
[23] a) A. de Juan, R. Tauler, *Anal. Chim. Acta* **2003**, *500*, 195 – 210; b) R. Tauler, *Chemom. Intell. Lab. Syst.* **1995**, *30*, 133 – 146.
[24] N. Kitajima, K. Fujisawa, C. Fujimoto, Y. Morooka, S. Hashimoto, T. Kitagawa, K. Toriumi, K. Tatsumi, A. Nakamura, *J. Am. Chem. Soc.* **1992**, *114*, 1277 – 1291.
[25] B. J. Hathaway, D. E. Billing, *Coord. Chem. Rev.* **1970**, *5*, 143 – 207.
[26] a) J. A. Halfen, S. Mahapatra, E. C. Wilkinson, S. Kaderli, V. G. Young, L. Que, A. D. Zuberbühler, W. B. Tolman, *Science* **1996**, *271*, 1397 – 1400; b) L. Q. Hatcher, M. A. Vance, A. A. Narducci Sarjeant, E. I. Solomon, K. D. Karlin, *Inorg. Chem.* **2006**, *45*, 3004 – 3013; c) S. Mahapatra, J. A. Halfen, E. C. Wilkinson, G. Pan, C. J. Cramer, L. Que Jr., W. B. Tolman, *J. Am. Chem. Soc.* **1995**, *117*, 8865 – 8866.
[27] V. Briois, C. L. Fontaine, S. Belin, L. Barthe, M. Th, V. Pinty, A. Carcy, R. Girardot, E. Fonda, *J. Phys. Conf. Ser.* **2016**, *712*, 012149.
[28] C. Lesage, E. Devers, C. Legens, G. Fernandes, O. Roudenko, V. Briois, *Catal. Today* **2019**, *336*, 63 – 73.

Manuscript received: January 24, 2020
Accepted manuscript online: March 2, 2020
Version of record online: May 14, 2020

